Angle-Resolved Polarized Raman Study of Layered b-As_xP_{x-1} Alloys: Identification of As-P Vibrational Modes

Mohammed Irziqat[a], Hiruni Weerahennedige[a], Dinushika Vithanage[a], Kazi Jannatul Tasnim[a], Md Rajib Khan Musa[a], Hansaka Weerarathne[a], Gamini Sumanasekera[a,b], Jacek B. Jasinski[b], and Ming Yu[a]*.*

Authors /Affiliations

Mohammed Irziqat, Hiruni Weerahennedige, Dinushika Vithanage, Kazi Jannatul Tasnim, Md Rajib Khan Musa, Hansaka Weerarathne, Gamini Sumanasekera, Ming Yu.

a) Department of Physics and Astronomy, University of Louisville, Louisville, KY, 40292, United States

Jacek B. Jasinski

b) Conn Center for Renewable Energy Research, University of Louisville Louisville, KY, 40292, United States

Abstract

In this study, the polarization-resolved Raman spectra of b-As_xP_{x-1} flakes with varying arsenic concentration (x = 0, 0.4, and 0.8) are systematically investigated. A clear polarization dependence is observed in the Raman intensity of all the P-P, As-P, and As-As modes and confirmed by the first-principles calculations. The observed angle-dependence can be related to the structure of the Raman tensors of each peak. In particular, the Raman intensities corresponding to As-P vibration modes are studied in detail. The out of plane As-P mode (A_g^1) is clearly identified, but the butterfly-shaped behavior observed in the polar plot around 350 cm^{-1} is interpreted as the combination of the two in-plane vibrations, one along the armchair and the other along the zigzag direction. This work allows unambiguous assignment of the A_g^1, B_{2g}, and A_g^2 modes of the As-P vibrational modes and the importance of the consideration of the superposition of the in-plane B_{2g} and A_g^2 modes. Such study can be utilized to further characterize the anisotropic structural properties and analyze the local distribution of the As and P in $b - As_xP_{1-x}$ alloys which will play key roles in electronic and optical properties. This methodology can be further extended to alloyed two-dimensional material systems with in-plane anisotropy in general.

Keywords: Angle-Resolved Polarized Raman Spectroscopy, alloys, b-As_xP_{x-1}, 2D materials, black arsenic phosphorous

1. INTRODUCTION

In recent years, black phosphorus (BP), a highly anisotropic two-dimensional (2D) material, has garnered significant attention due to its remarkable properties and broad range of potential applications [1-3]. In particular, BP exhibits properties such as thickness-dependent wide tunability of the bandgap (from 0.3 eV to 2 eV)[4] , strong in-plane anisotropy [5], high carrier mobility [6], as well as noteworthy optical [7] and thermal properties [8]. These properties can be further refined or enhanced by partially substituting phosphorus with arsenic in the crystal lattice, resulting in the formation of black arsenic-phosphorus (b-As_xP_{1-x}) alloys. Notably, alloying stands as one of the most effective band engineering strategies, pivotal in adjusting the electronic and optical properties of 2D materials, which is significant for their utilization in electronics, optoelectronics, and energy conversion [9, 10]. Alloying enables the fine-tuning of the bandgap to create materials with enhanced light absorption or emission properties, pivotal in applications like solar cells or light-emitting diodes (LEDs). Furthermore, it influences the charge carrier mobility and doping behavior of 2D materials, thereby potentially boosting the performance of these materials in electronic devices.

Across a broad range of compositions ($x \leq 0.83$), the alloying of phosphorus with arsenic maintains the orthorhombic honeycomb puckered crystal structure of BP, identified by the *Cmca* space group. As the As concentration increases from x=0 to 0.83, there is a nearly linear increase in the lattice parameters [11, 12] and a reduction in the bandgap from 0.3eV in BP to 0.15eV in b-$As_{0.83}P_{0.17}$, for bulk materials [13]. Moreover, arsenic alloying can enhance various properties, as demonstrated in our recent study highlighting the exceptional electrical transport properties of certain b-As_xP_{1-x} alloys [12]. Other studies indicate the high carrier mobilities of such alloys [14], rendering them promising materials for electronic applications, or exhibiting good Coulombic

efficiencies and potential use in Li-ion batteries [15]. Furthermore, the introduction of As atoms into the BP lattice can improve its environmental stability, as illustrated in our recent study where nearly a three-fold stability improvement for b-$As_{0.4}P_{0.6}$ was observed compared to BP [16]. Altogether b-As_xP_{1-x} have exotic properties and interesting applications, which requires more insight studying.

Since the introduction of graphene in 2004, Raman spectroscopy has been increasingly and routinely used to study and characterize different kinds of 2D materials [17]. It can provide information on stacking order [18], layer thickness [19], surface adsorbates [20], strain effects [21] etc. However, its variant, angle-resolved polarized (ARP) Raman spectroscopy has emerged as a powerful tool in the research of optically anisotropic 2D materials. By changing the polarization of incident or scattered light or both, ARP Raman spectroscopy can provide invaluable insight about these intricate 2D materials. More importantly, the analysis of the angle-resolved experiments provides the determination of the Raman tensor elements of the 2D crystal [22, 23]. Nowadays, there is growing interest in the study of optically anisotropic 2D materials by ARP Raman spectroscopy since the unusual results in layered black phosphorus (BP) were explained by Ribeiro et al [24]. Moreover, Jungcheol et al. investigated polarization dependence of Raman modes in BP by ARP Raman spectroscopy [25]. They showed that the ARP Raman intensities of A^1_g and A^2_g vibrational modes depend on sample's thickness and excitation wavelength, but not for B_{2g}. Yanming Zhu et al. studied polarization dependence of BP Raman modes on the basal and edge plane and concluded that the strong observed Raman anisotropy stems mainly from varying differential polarizability along different directions [26]. Miao-Ling Lin et al. developed a so-called birefringence-linear-dichroism (BLD) model to qualitatively understand ARP Raman intensity at both normal and oblique laser incidences. They used BP as a prototype and used the

BLD model to understand its ARP Raman intensity. In this approach, they used real number elements in the Raman tensors for certain laser excitation [27]. Despite several studies published on the polarized Raman spectroscopy of BP, there is limited information in the literature on polarized Raman spectroscopy of b-As_xP_{1-x} [13, 28, 29]. Hence, detailed analysis of ARP Raman measurements of b-As_xP_{1-x} by measuring and comparing angle-resolved Raman measurements of different arsenic concentration is provided in this work. Especially, the unambiguous assignment of the Raman peaks of the two in-plane vibrational modes of the As-P modes (B_{2g} and A_g^2) has not been clearly addressed. In this study, the anomalous shape observed in the intensity polar plot of the in-plane vibrational modes of As-P vibrational modes is addressed.

2. METHODS

2.1 Synthesis of BP and b-As_xP_{1-x}

A chemical vapor transport (CVT) technique was utilized to synthesize BP and b-As_xP_{1-x} alloys, as described in our previous work [12]. Briefly, red phosphorus (Sigma, 97%) and gray arsenic (Sigma, 99.99%) were combined in stoichiometric amounts (molar ratios), totaling 300 mg, within a quartz ampoule. In addition, Sn (10 mg, Alfa Aesar, 99.8%) and SnI_4 (5 mg, Alfa Aesar, > 95%) were added as mineralizing agents. The ampule was then evacuated to 10^{-6} Torr and sealed using an oxy-acetylene flame torch. Then those sealed quartz ampoules were annealed at 650 °C, maintaining a temperature gradient of 50 °C between hot and cold ends in a two-zone furnace. A proper temperature profile was maintained to ensure high-quality crystals. BP was synthesized without the use of any gray As.

2.2 Characterization of BP and b-As_xP_{1-x} samples

Several characterization techniques were employed to verify the structure and quality of the synthesized As_xP_{1-x} samples. Raman spectroscopy, utilizing a Renishaw inVia spectrometer with a 632 nm He−Ne laser, was used to study the atomic vibrational modes. To assess the crystal structures and measure the lattice parameters of the synthesized samples, X-ray diffraction spectra using the Bruker Discover 8 were obtained and analyzed. Transmission electron microscopy (TEM) and energy-dispersive X-ray spectroscopy, using the FEI Tecnai F20 TEM equipped with an EDAX TEAM EDS spectrometer, were employed to obtain information about the morphology and elemental composition of the synthesized samples. The results of these measurements are reported in our recent works [12, 30].

2.3 Angle-Resolved Polarized (ARP) Raman Spectroscopy

The polarization vector $\vec{P}$ induced in a material due to a laser beam with the electric field $\vec{E}^i$ incident on the surface of a crystal can be written, in the linear regime, by the expression $\vec{P} = \varepsilon_0 \overleftrightarrow{\chi} \vec{E}^i$, where ε_0 is the electric permittivity of free space, and $\overleftrightarrow{\chi}$ is the second-rank tensor electric susceptibility, characterizing the response of the vectors $\vec{P}$ and $\vec{E}^i$. Consequently, light will be emitted in different directions by this oscillating induced polarization. Most of the emitted light is elastically scattered (Rayleigh scattering) but a small fraction of the light is inelastically scattered due to the production or destruction of phonons, giving rise to the Raman scattering process.

Each cartesian component of the electric susceptibility tensor χ_{ij} can be modulated by a vibrational mode μ described by the generalized normal coordinate q^μ. If the polarization vector $\vec{e}^i$ of the incident light is represented by a 3 x 1 column matrix while the polarization vector $\vec{e}^s$ of the scattered light is represented by a 1 x 3 raw matrix, the intensity of the Raman scattered light can be evaluated from the Raman tensor R^μ of a mode μ as follows [24]:

$$I \propto \left| (e_x^s \quad e_y^s \quad e_z^s) \begin{pmatrix} R_{xx}^{\mu} & R_{xy}^{\mu} & R_{xz}^{\mu} \\ R_{yx}^{\mu} & R_{yy}^{\mu} & R_{yz}^{\mu} \\ R_{zx}^{\mu} & R_{zy}^{\mu} & R_{zz}^{\mu} \end{pmatrix} \begin{pmatrix} e_x^i \\ e_y^i \\ e_z^i \end{pmatrix} \right| \quad \textbf{(1)}$$

Where $R_{ij}^{\mu} = \dfrac{\partial \chi_{ij}}{\partial q^{\mu}}$.

Since the influence on the incident and scattered light by the different optical components along their paths of a Raman system is not exactly known, we use the proportionality symbol. Equation (1) is the starting point for any angle-resolved polarized Raman measurements. It also shows that the intensity is dependent not only on the structure of Raman tensor but also on the polarization directions of incident and selected Raman scattered light.

Figure 1(a) shows the setup used in the ARP Raman measurements in this study. It is based on the simultaneous modulation of the incident and Raman back-scattered lights [23, 31]. To do this, a half-wave plate (HWP) was inserted in the common path of the incident and scattered light before the microscope objective. By rotating the HWP by an angle $\theta/2$, the polarization vectors of incident and Raman scattered light are rotated by an angle of θ. Usually, two polarization configurations of the incident and the selected Raman scattered light are needed in ARP Raman measurements: parallel and perpendicular configurations. The parallel configuration corresponds to $\vec{e}^{\,i}$ and $\vec{e}^{\,s}$ pointing in the same direction. Whereas in the perpendicular configuration, $\vec{e}^{\,i}$ and $\vec{e}^{\,s}$ are normal to each other. In Figure 1(a), $\vec{e}^{\,i}$ is represented by red-colored two-way arrow, whereas $\vec{e}^{\,s}$ is represented by orange-colored two-way arrow. Under this type of ARP Raman measurement, the intensity of the Raman scattered light as a function of θ then becomes:

$$I \propto \left| \vec{e}^{\,s} \cdot J_{HWP} \cdot R^{\mu} \cdot J_{HWP} \cdot \vec{e}^{\,i} \right|^2 \quad \textbf{(2)}$$

where J_{HWP} is the jones matrix of the HWP in the x-y plane of the laboratory coordinate system, which takes the form:

$$J_{HWP} = \begin{pmatrix} -cos(\theta) & sin(\theta) & 0 \\ sin(\theta) & cos(\theta) & 0 \\ 0 & 0 & 0 \end{pmatrix}$$

However, since the crystal coordinate system does not necessarily coincide with the laboratory coordinate system (Figure 1(b)), the Raman tensor needs to be transformed to the laboratory coordinate system by the equation: $M \cdot R^{\mu} \cdot M^{T}$, where M is *x-y* rotation matrix given by:

$$M = \begin{pmatrix} -cos(\beta) & \sin(\beta) & 0 \\ \sin(\beta) & \cos(\beta) & 0 \\ 0 & 0 & 1 \end{pmatrix} \quad .$$

So, equation (2) above becomes:

$$I \propto \left| \vec{e}^{\,s} \cdot J_{HWP} \cdot M^{T} \cdot R^{\mu} \cdot M \cdot J_{HWP} \cdot \vec{e}^{\,i} \right|^2 \qquad \textbf{(3)}$$

with $\vec{e}^{\,i} = (0 \quad 1 \quad 0)^T$ and $\vec{e}^{\,s} = (0 \quad 1 \quad 0)$ for parallel configuration; $\vec{e}^{\,i} = (0 \quad 1 \quad 0)^T$ and $\vec{e}^{\,s} = (1 \quad 0 \quad 0)$ for perpendicular (cross) configuration, respectively.

For an orthorhombic crystal structure like black phosphorus and its arsenic alloys with arsenic compositions below approximately x = 0.83, the Raman tensors of the A_g (including A_g^1 and A_g^2) and B_{2g} modes can be expressed as follows [31]:

$$R^{A_g} = \begin{pmatrix} ae^{i\varphi_a} & 0 & 0 \\ 0 & ce^{i\varphi_b} & 0 \\ 0 & 0 & be^{i\varphi_c} \end{pmatrix}, \; R^{B_{2g}} = \begin{pmatrix} 0 & fe^{i\varphi_f} & 0 \\ fe^{i\varphi_f} & 0 & 0 \\ 0 & 0 & 0 \end{pmatrix}$$

Then the angle-dependent Raman intensities for the A_g (including A_g^1 and A_g^2) and B_{2g} under parallel and cross configurations are given by the following equations:

Parallel Configuration:

$$I_{\parallel}^{A_g}(\theta) \propto \frac{1}{8}(3\,a^2 + 3\,c^2 + 2\,a\,c\,cos(\emptyset_{ac}) - a\,c\,cos(\emptyset_{ac} + 4\,\beta\, - 4\,\theta) - 4\,(a^2 - c^2)\,cos\big(2(\beta - \theta)\big) + (a^2 + c^2)\,cos\big(4\,(\beta - \theta)\big) - a\,c\,cos\,(\emptyset_{ac} - 4\beta + 4\theta) \quad \textbf{(4)}$$

where $\varphi_{ac} = \varphi_a - \varphi_c$.

$$I_{\parallel}^{B_{2g}}(\theta) \propto f^2(sin\,(2(\beta - \theta)))^2 \quad \textbf{(5)}$$

Cross Configuration:

$$I_{\perp}^{A_g}(\theta) \propto \frac{1}{4}(\,a^2 + c^2 - 2\,a\,c\,cos(\emptyset_{ac}))(sin\,(2(\beta - \theta)))^2) \quad \textbf{(6)}$$

$$I_{\perp}^{B_{2g}}(\theta) \propto f^2(cos\,(2(\beta - \theta)))^2 \quad \textbf{(7)}$$

When the laboratory coordinate system coincides with the crystal coordinate system; $\beta = 0$, equations (4)-(7) reduce to:

$$I_{\parallel}^{A_g}(\theta) \propto (a\,sin^2(\theta) + c\,cos^2(\theta)\,cos\,\phi_{ac})^2 + c^2\,cos^4(\theta)\,sin^2\,\phi_{ac} \quad \textbf{(8)}$$

$$I_{\parallel}^{B_{2g}}(\theta) \propto (2f\,sin(\theta)\,cos(\theta))^2 \quad \textbf{(9)}$$

$$I_{\perp}^{A_g}(\theta) \propto [(a - c\,cos\,\phi_{ac})^2 + c^2\,sin^2\,\phi_{ac}]\,sin^2(\theta)\,cos^2(\theta) \quad \textbf{(10)}$$

$$I_{\perp}^{B_{2g}}(\theta) \propto \big(f\,cos\big(2(\theta)\big)\big)^2 \quad \textbf{(11)}$$

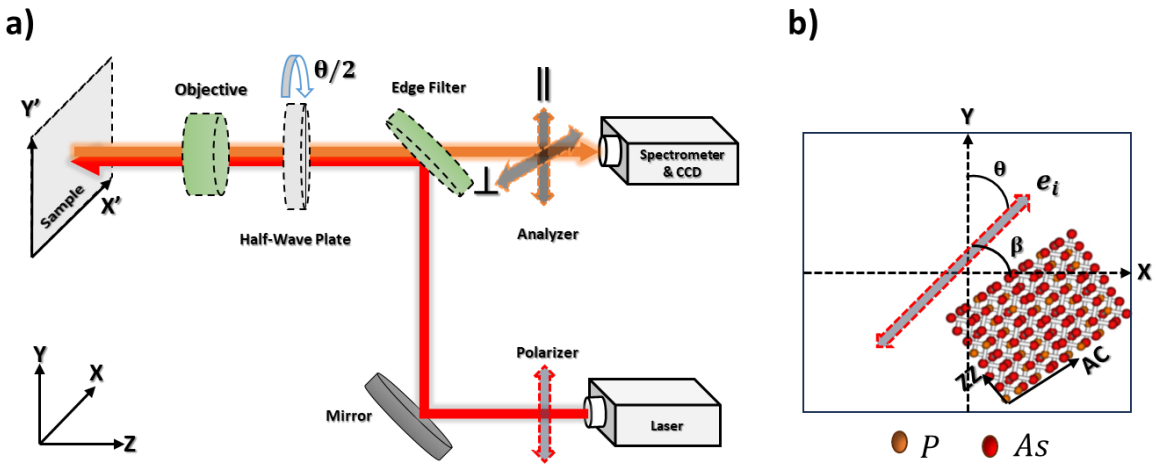

Figure 1. (a) Schematic diagram of the angle-resolved polarized Raman setup where ∥ and ⊥ refer to the directions of analyzer for the parallel (along Y-axis) and cross (along X-axis) configurations, respectively. Laboratory coordinates (xyz) and crystal coordinates (x'y'z') are represented by black arrows. The two coordinate systems coincide with each others. Red-dashed two-way arrow stand for the incident laser polarization just before the HWP. Orange-dashed two-way arrows represent the selected polarization of Raman signal by the analyzer before spectrometer entrance. (b) As_xP_{1-x} alloy with a coordinate system that doesn't coincide with the laboratory coordinate system. The red-dashed two-way arrow there represents the direction of polarization of incident light reaching the sample.

Figure S1 in the supporting document shows calculated intensities of ARP Raman spectra for A_g^1, B_{2g}, and A_g^2 modes of BP under parallel and cross configurations using equations (8)-(11). Those results agree with experimental results reported in the literature [24, 32].

In this study, we preformed the ARP Raman measurements on the b-As_xP_{1-x} flakes using a Renishaw inVia microRaman system operating at 632 nm (He-Ne laser). The laser power was kept below 0.8 mW to avoid sample heating effects. A 50X objective (NA=0.75) was used to focus incident light and simultaneously collect Raman scattered light. The back-scattered light was dispersed on a CCD camera using a 1200 g/mm grating. Because the light intensity dispersed by the spectrometer depends on light polarization, we have fixed the light polarization entering the spectrometer for both parallel and cross configurations. To achieve this, a fixed polarizer with a transmission axis at 0^0 with respect to the Y-axis (as shown in Figure 1(a)) is positioned just before the spectrometer entrance for parallel-polarization configuration measurements. For cross - polarization configuration measurements, a fixed half-wave plate with its fast-axis oriented at 45^0

with respect to the transmission axis of the polarizer is placed in front of the polarizer. This combination of the half-wave plate and polarizer is equivalent to rotating the polarizer by 90 degrees.

2.1 Sample Preparation for ARP Raman Measurements

After synthesis of samples by CVT methods, flakes were mechanically exfoliated using scotch tape and then transferred onto a microscope slide for ARP Raman measurements. The flakes were multilayers with a number of layer larger than 10 for each sample. Figure S2 shows optical images of such flakes.

2.4 Theoretical Calculations

The analysis of polarized Raman spectra for b-As_xP_{1-x} alloys were carried out using the density functional theory (DFT) implemented in the Vienna ab initio simulation package [33], with a plane wave basis set code. The electron-ion interaction was characterized by the projector augmented wave (PAW) algorithm [34], and the Perdew–Burke–Ernzerhof (PBE) [35] generalized gradient approximation (GGA) approach [36] was utilized for the exchange-correlation functional. The initial atomic structure of b-As_xP_{1-x} alloy was optimized starting from black phosphorus, with a 1x1x1 rectangular unit cell containing 8 P atoms (optimized lattice constants: a = 3.33 Å, b = 11.18 Å, c = 4.52 Å). The constructed structure configurations were optimized by replacing P atoms with As atoms arbitrarily within the unit cell. There are $8!/n!\,(8-n)!$ possible configurations to substitute n P atoms with n As atoms when there is 8 P atoms per unit cell. A full structural relaxation process using the Conjugate Gradient algorithm [37] was then performed for all constructed configurations, with no constraints on the unit cell volume, shape, or atomic positions. The reciprocal space was sampled using gamma-centered 11x7x11 k-point mesh based on Monkhorst scheme [38] during the relaxation calculation. A cutoff energy of 270 eV was applied

for all calculations, with energy and force convergent criteria set at 10^{-6} eV and 10^{-5} eV/Å, respectively. The van der Waals interactions were taken into account using the zero damping DFT-D3 method proposed by Grimme et. al [39]. The Raman shifts of these systems were calculated within the double harmonic approximation from the lattice vibrational frequencies that were extracted by diagonalizing the Hessian matrix and the dipole moment and the polarizability (and their derivatives) with respect to the atomic coordinates determined by a finite differencing of energies and forces with respect to the electric field [40, 41] (Fig. S4). The intensity of the angle-dependent polarized Raman modes was calculated using equations (4)-(11) and the corresponding parameters were extracted from the Raman tensors obtained from the Raman shift calculations (Table S1). Calculated results are consistent with the experimental data (Figs. S5-S7).

3. RESULTS AND DISCUSSION

Normal Raman spectra, acquired at room temperature, for BP and two distinct b-As_xP_{1-x} alloys (b-$As_{0.4}P_{0.6}$ and b-$As_{0.8}P_{0.2}$), are shown in Figure 2. Samples were selected to encompass three As concentrations (x=0, 0.4, and 0.8), deliberately chosen to allow analysis across the spectrum, from the endpoints to the midpoint. Within the compositional range ($0 \leq x \leq \sim 0.83$), arsenic-phosphorus alloys exhibit their α phase, characterized by an orthorhombic honeycomb puckered crystal structure and the space group *Cmca* [12, 37]. As As concentrations increase beyond ~0.83, the arsenic-phosphorus alloys transition to the β phase, distinguished by a rhombohedral buckled layered crystal structure with the space group *R3m* [42].

The active Raman modes (i.e., A_g^1 ,B_{2g} , and A_g^2 modes) of b-As_xP_{1-x} alloys are illustrated in Figure S3 and corresponding frequencies for each mode are listed in Table 1. It was found that as the arsenic concentration of the alloy increases, a decrease in peak intensities for P-P vibrational modes (around 350 cm^{-1} – 470 cm^{-1}) were observed, whereas peak intensities corresponding to As-As

vibrations (around 220 cm^{-1} – 260 cm^{-1}) were increased. It is reasonable because P-P vibrations become less prominent when more P atoms are replaced by As atoms in the lattice. It is also observed that peaks of alloy samples are red shifted (w.r.t BP sample) with increasing arsenic concentration. This finding is in accordance with a volume expansion associated with the increasing amount of As-As bonds and the decreasing contribution of P-P bonds, as well as the change in bond strength and bond lengths in the system upon arsenic substitution. With increasing arsenic concentration, the As-P peaks appear in the middle frequency regime (around 300 cm^{-1} – 350 cm^{-1}). We also calculated the Raman spectra of b-As_xP_{1-x} systems and found that the As-P peaks are predicted to occur in the range from 300 to 350 cm^{-1}, showing good agreement with the experimental observations.

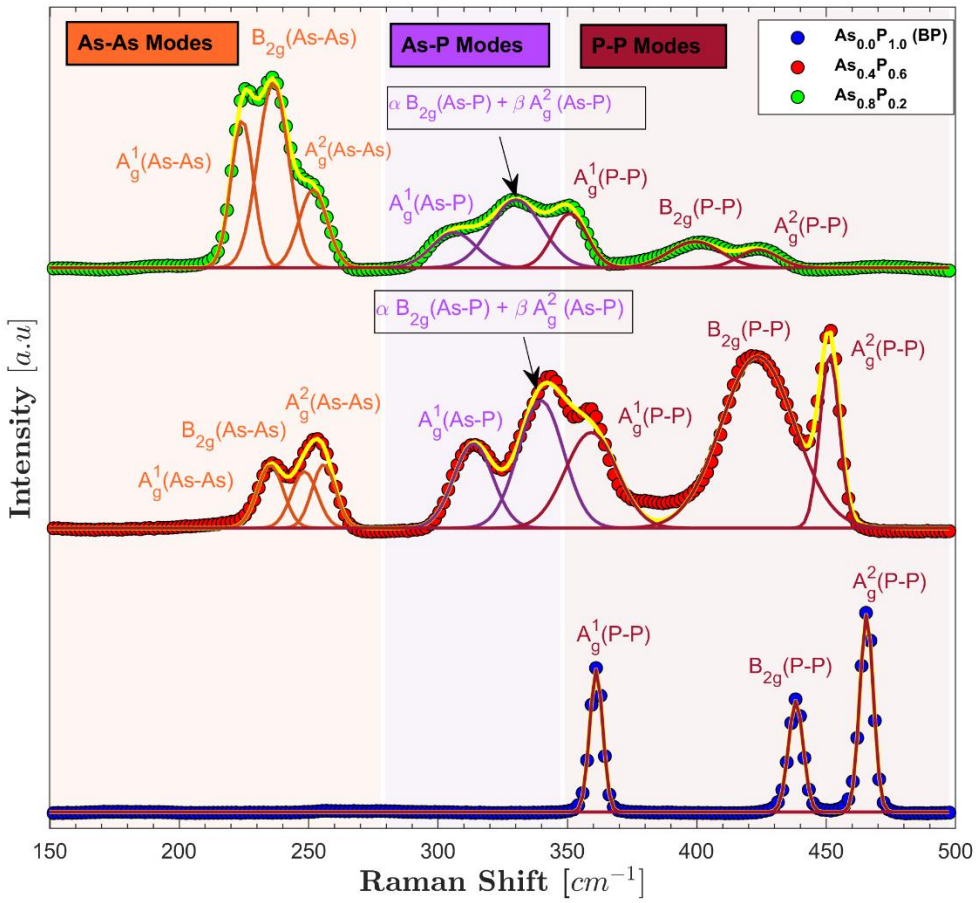

Figure 2. Experimental non-polarized Raman spectra for pristine BP (blue color), and b-As_xP_{1-x} alloys with two different chemical compositions (red and green). Yellow curves correspond to the total Gaussian fits of the individual peaks where orange-, purple-, and wine-colored peaks correspond to As-As, As-P, P-P modes. Interpretation for using the linear combination of the two modes (B_{2g} , and A_g^2) will be given later in the manuscript.

System	Vibration modes	A_g^1	B_{2g}	A_g^2
BP	P-P	361.11 cm^{-1}	438.23cm^{-1}	465.57cm^{-1}
As0.4P0.6	P-P	359.30 cm^{-1}	421.06 cm^{-1}	451.75cm^{-1}
	As-P	312.63 cm^{-1}	342.05 cm^{-1}	
	As-As	235.96 cm^{-1}	249.96 cm^{-1}	255.20 cm^{-1}
As0.8P0.2	P-P	350.68 cm^{-1}	400.53 cm^{-1}	424.48 cm^{-1}
	As-P	303.96 cm^{-1}	328.22 cm^{-1}	
	As-As	225.45 cm^{-1}	235.96 cm^{-1}	251.71 cm^{-1}

Table 1. Frequencies of each Raman modes for BP, $As_{0.4}P_{0.6}$, and $As_{0.8}P_{0.2}$ alloys.

Angle-resolved polarized (ARP) Raman spectroscopy is a very important branch of Raman spectroscopy to study the orientation of Raman modes induced by the Raman tensor and hence to provide the precise determination of phonon polarization properties of different planes of layered system and crystal symmetry and orientation, which are an essential prerequisite for understanding and tuning the interplay between the geometrical structure of layered materials and its optical and electronic properties. Figure 3 shows ARP Raman spectra of BP at various polarization angles (θ) from 0° to 360° at 20° increments under parallel configuration (Figure 3 (a)) and cross configuration (Figure 3 (b)), respectively. The intensity maps of the three peaks (A_g^1, B_{2g} and A_g^2) are shown below each graph. It is found that the intensities of A_g^1, B_{2g} and A_g^2 modes for P-P vibrations are sensitive to the polarization angles and configurations.

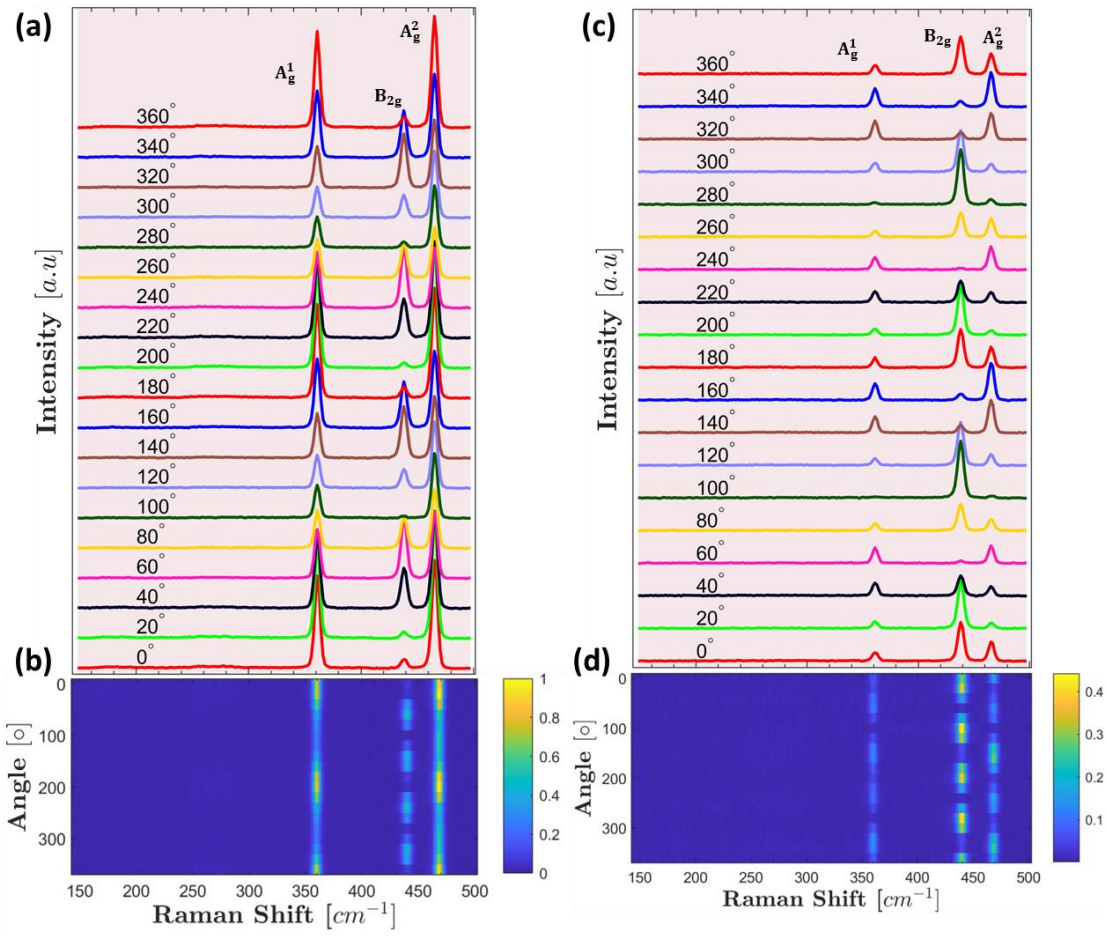

Figure 3. Polarization-dependent Raman spectra of a BP sample at different polarization angles from 0° to 360° at 20° increments for (a) parallel configuration (c) cross configuration. (b) and (d) show intensity maps of the three Raman modes for parallel and cross configuration, respectively.

Figure 4 shows the polar plots of normalized ARP Raman intensities of all three A_g^1 ,B_{2g} and A_g^2 modes of BP as the polarization angle θ varies from 0 to 360° at 20° increments. The solid circles are experimental data that are fitted by the intensity function of each mode (equations. (4)-(7)) derived using corresponding Raman tensors for an orthorhombic crystal structure (solid lines). The fits with equations (4)-(7) are in excellent agreement with the experimental results and the fitted

parameters for the Raman tensors are listed in Table S2. The intensities of ARP Raman modes under the parallel configuration are greater than those under the cross configuration, and the intensities of A_g^1 and A_g^2 modes are stronger than that of B_{2g} mode under the parallel configuration but opposite under the cross configuration. Furthermore, the angle-dependent intensity shapes are significantly different under the parallel and cross configurations. In the case of the parallel configuration (Figure 4 (a)), the normalized intensity of the A_g^1 mode reaches the maximum at 0^0 and 180^0 degrees and the minimum around 90^0 and 270^0 degrees, showing a dumbbell shape horizontally. Similar behavior is also found in the A_g^2 mode but with a smooth bumper around 90^0 and 270^0 degrees, showing anisotropic feature. The intensity of B_{2g} mode, on the other hand, reaches maximum around 45^0, 135^0, 225^0, and 315^0 degrees, but minimum at 0^0, 90^0, 180^0, and 270^0, showing a four-leaf clover shape. For the cross configuration (Figure 4 (b)), on the other hand, such four-leaf clover shape keeps in all three polarized Raman modes except a 90^0 rotation with respect to the B_{2g} mode under the parallel configuration. These observed polarization angle-dependent Raman spectra are consistent with the calculated results (Figure S1) and the reported results[24, 26, 32]. As the A_g^1 characterizes the out-of-plane vibration and the A_g^2 (B_{2g}) characterizes the in-plane vibration along the armchair (zigzag) direction, the ARP Raman results clearly reveal the anisotropic feature of BP crystal structure.

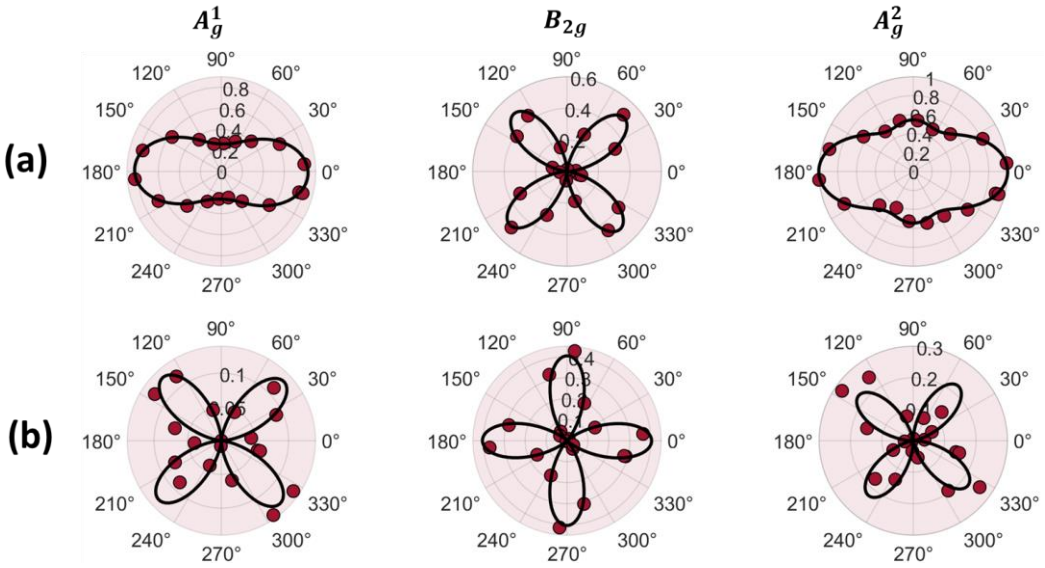

Figure 4. Polar plots of normalized Raman intensities of all three A_g^1, B_{2g} and A_g^2 modes of BP in (a) parallel configuration (b) cross configuration. The solid circles are the experimental data that are fitted by the intensity function of each mode derived using corresponding Raman tensors for an orthorhombic crystal structure (solid lines).

As the phosphorus atoms are randomly replaced by the arsenic atoms forming b-As_xP_{1-x} alloys, the Raman modes associated with As-P and As-As vibrations appear in the low frequency regions (i.e., around 300-350 cm^{-1} for As-P and around 200-250 cm^{-1} for As-As, respectively). Figure 5 shows ARP Raman spectra of b-$As_{0.4}P_{0.6}$ sample at different polarization angles from 0° to 360° at 20° increments for (a) parallel configuration (b) cross configuration, respectively. The intensity maps of the three peaks are shown below each graph. These new results provide further information about the anisotropic structure of b-As_xP_{1-x} alloys and the local distribution of As and P atoms through the analysis of the strength of the intensities of As-P vibration modes.

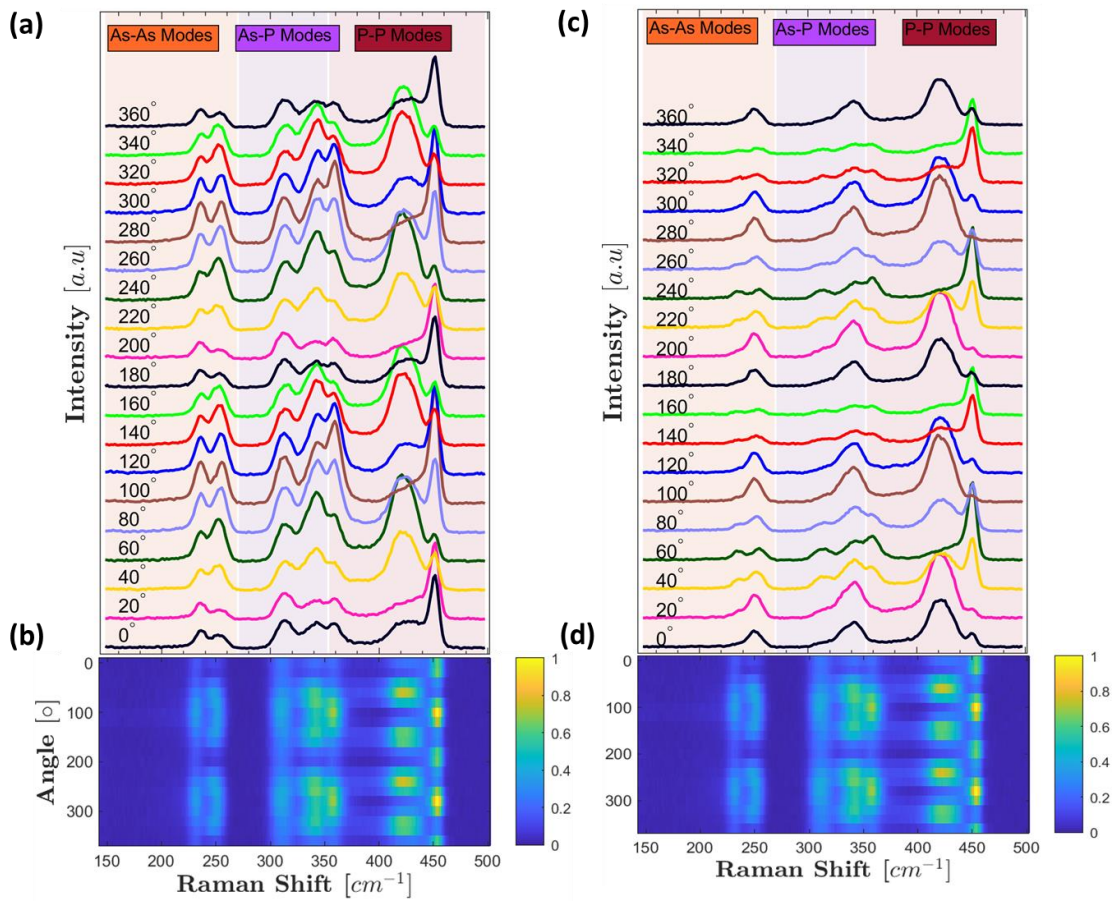

Figure 5. Polarization-dependent Raman spectra of b- $As_{0.4}P_{0.6}$ sample at different polarization angles from 0° to 360° at 20° increments for (a) parallel configuration (c) cross configuration. (b) and (d) show intensity maps of the three Raman modes for parallel and cross configuration, respectively.

Figure 6 shows the normalized polar plots of Raman intensities of three A_g^1 , B_{2g} and A_g^2 P-P vibrational modes (bottom panels), two As-P modes (middle panels), and three A_g^1 , B_{2g} and A_g^2 modes of As-As modes (upper panels) of b-$As_{0.4}P_{0.6}$ sample in (a) parallel configuration (b) cross configuration. The solid circles are the experimental data that are fitted by the intensity function

of each mode derived using Raman tensors for an orthorhombic crystal structure (solid lines). Again, the intensity strength is higher in the parallel configuration than in the cross configuration. The angle-dependent intensities of ARP Raman A_g^1 , B_{2g} and A_g^2 modes corresponding to P-P vibrations maintain the same feature as found in BP with pronounced anisotropic properties of A_g^2 in the parallel configuration and A_g^1 modes in the cross configuration, respectively (Figure 6 (a) and figure 6 (b) in the bottom panels). Similar feature also found in three As-As vibrational modes (upper panels in Figure 6 (a) and (b)), except that (1) the anisotropic behavior found in A_g^2 mode of P-P vibration in parallel configuration is weakened in the As-As vibration, and (2) the four-leaf clover shape in B_{2g} mode of P-P vibration in the parallel configuration is smoothed out in As-As vibration. More interesting, there are two pronounced peaks in the region of 300 cm^{-1} -350 cm^{-1} which are identified as ARP Raman modes of As-P bonds vibration. The dumbbell shape in the parallel configuration around 300 cm^{-1} characterizing the feature of A_g^1 mode, but the butterfly shape in the parallel configuration around 350 cm^{-1} neither characterizes the four-leaf clover shape of B_{2g} mode nor the dumbbell shape of A_g^2 mode as found the P-P and As-As modes.

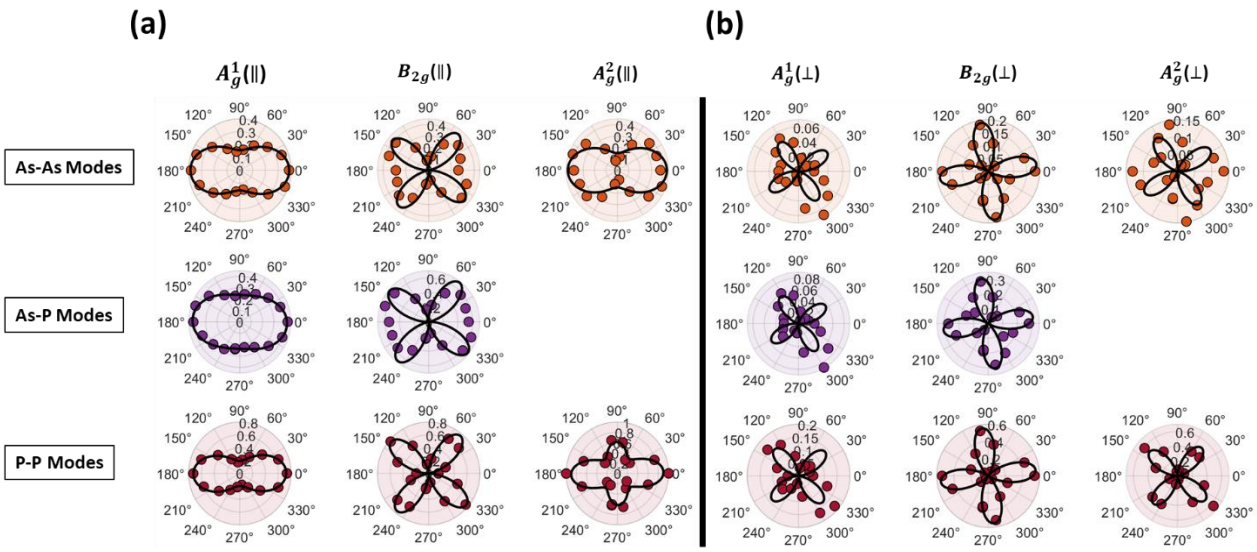

Figure 6. Polar plots of normalized Raman intensities of three A_g^1 ,B_{2g} and A_g^2 P-P vibrational modes, two As-P modes, and three A_g^1 ,B_{2g} and A_g^2 modes of As-As modes of b- $As_{0.4}P_{0.6}$ sample in (a) parallel configuration (b) cross configuration. The solid circles are the experimental data that are fitted by the intensity function of each mode derived using corresponding Raman tensors for an orthorhombic crystal structure (solid lines).

Similar trend is also found in b-$As_{0.8}P_{0.2}$ alloy. Figure 7 shows the ARP Raman spectra of b-$As_{0.8}P_{0.2}$ sample at different polarization angles from 0° to 360° at 20° increments for (a) parallel configuration (b) cross configuration. The intensity maps of the three peaks are shown below each graph. The polar plots of normalized Raman intensities of three A_g^1 ,B_{2g} and A_g^2 P-P vibrational modes (bottom panels), two As-P modes (middle panels), and three A_g^1 ,B_{2g} and A_g^2 modes (upper panels) of As-As modes of b-$As_{0.8}P_{0.2}$ sample in (a) parallel configuration (b) cross configurations were also presented in Figure 8. The solid circles are the experimental data that are fitted by the intensity function of each mode derived using Raman tensors for an orthorhombic crystal structure (solid lines).

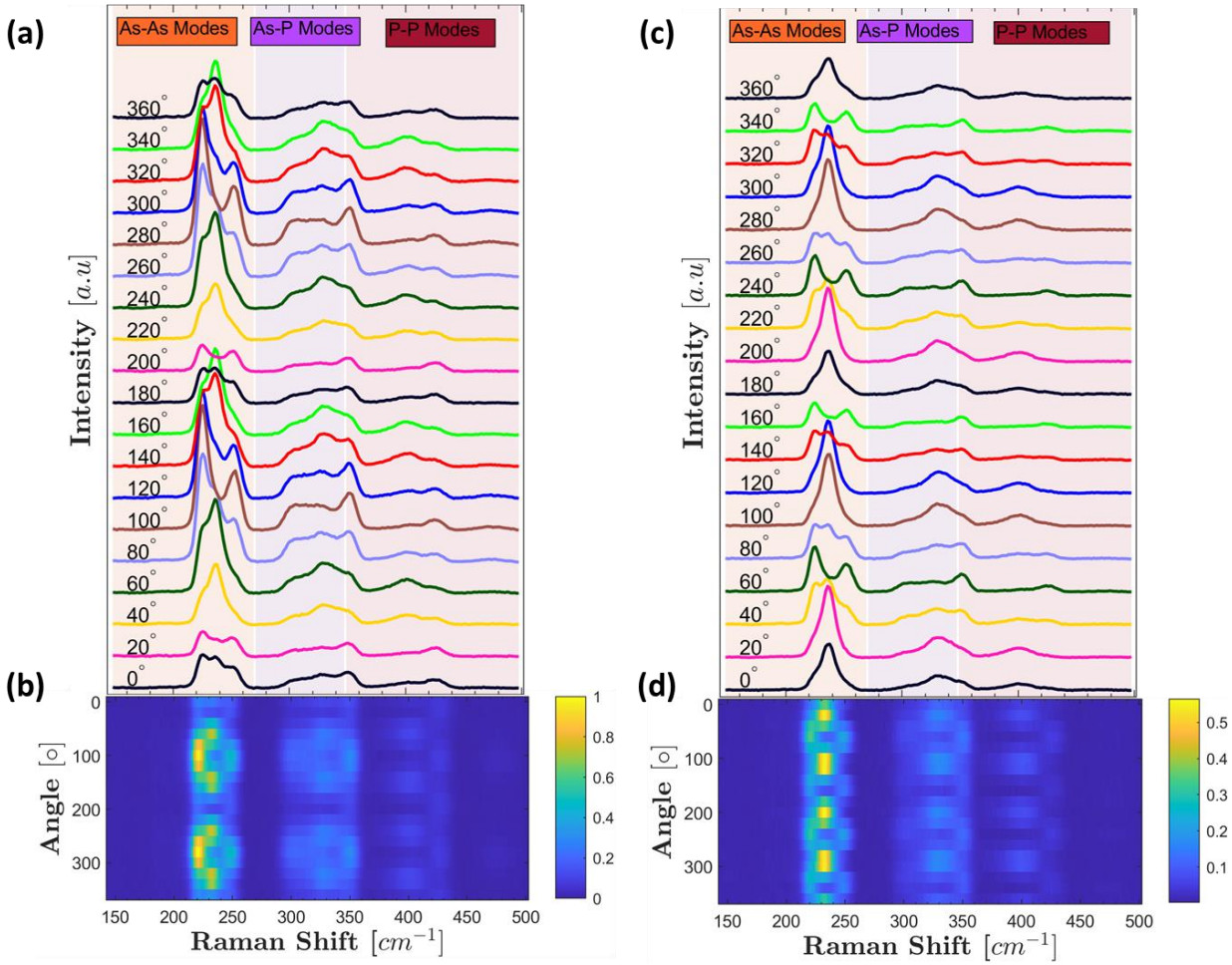

Figure 7. Polarization-dependent Raman spectra of b-$As_{0.8}P_{0.2}$ sample at different polarization angles from 0° to 360° at 20° increments for (a) parallel configuration (c) cross configuration. (b) and (d) show intensity maps of the three Raman modes for parallel and cross configuration, respectively.

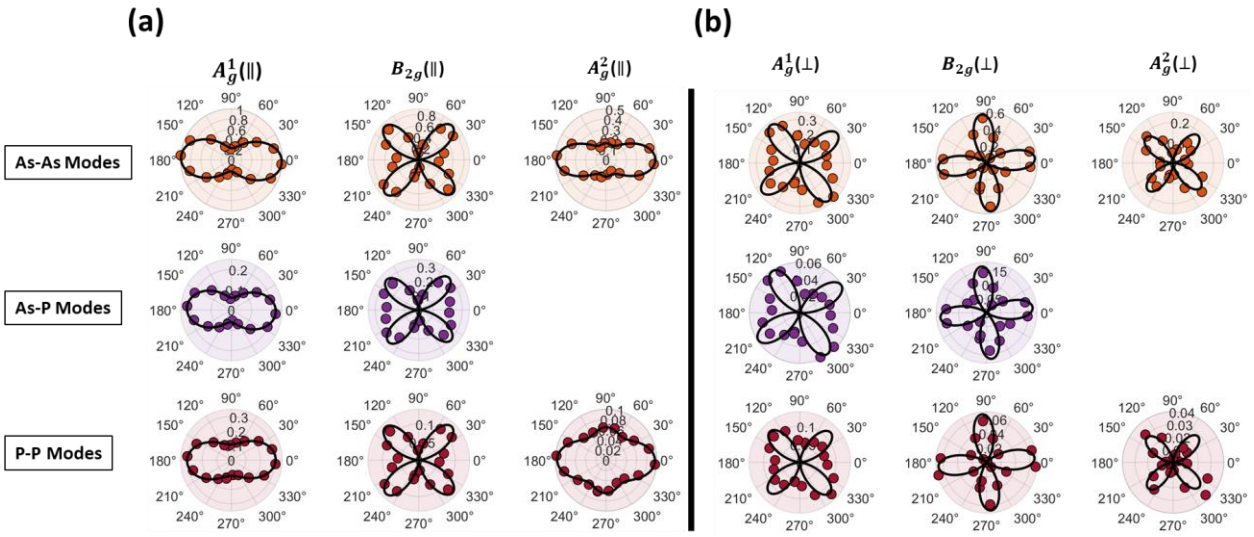

Figure 8. Polar plots of normalized Raman intensities of all three A_g^1 ,B_{2g} and A_g^2 P-P vibrational modes, two As-P modes, and three A_g^1 ,B_{2g} and A_g^2 modes of As-As modes of b-$As_{0.8}P_{0.2}$ sample in (a) parallel configuration (b) cross configuration. The solid circles are the experimental data that are fitted by the intensity function of each mode derived using Raman tensors for an orthorhombic crystal structure (solid lines).

To further confirm the observed ARP Raman data, we performed theoretical calculations. As shown in Figures S5-S7, calculated intensities (orange-solid curves) of ARP Raman spectra for all active Raman modes of BP and b-As_xP_{1-x} alloys are consistent with the fitted experimental data (blue-dashed curves). To understand the butterfly shape observed in the angle-dependent of Raman intensity of b-As_xP_{1-x} alloys in the parallel configuration around 350 cm^{-1}, we deeply analyzed the Raman intensities of the in-plane As-P vibrational modes along the armchair and the zigzag directions (i.e., B_{2g} and A_g^2) with different fittings. One is fitting from the intensity function

derived using Raman tensors for an orthorhombic crystal structure considering only one mode (e.g., B_{2g}or A_g^2 mode) and the other is fitting with a superposition of these two modes, as shown in Figure 9. The theoretical results of the DFT based calculations considering the superposition of the two modes are also shown. The excellent agreement of the experimental results with the theoretical fittings are seen when the superposition of the two in-plane modes for As-P vibrations is considered. Such results indicate a coexistence of the vibration frequencies around 350 cm ^{1}. By fine tune in fitting the Raman peaks around 350 cm^{-1}, it was found that there is indeed an overlapping peak in this region characterizing the two in-plane modes (blue-dashed curves in the middle and upper panels of Figure 9 (d)). The intensity of A_g^2mode (peak near 350 cm^{-1}) is slightly weaker than that of B_{2g}mode in b-$As_{0.4}P_{0.6}$ but opposite in b-$As_{0.4}P_{0.6}$ samples. Since the B_{2g} and A_g^2 modes characterize the in-plane As-P vibrations along the zigzag and armchair direction respectively, the difference in the intensity can be utilized to analyze the local distribution of As-P bonds along these directions, and therefore, the distribution of As and P atoms in the alloys.

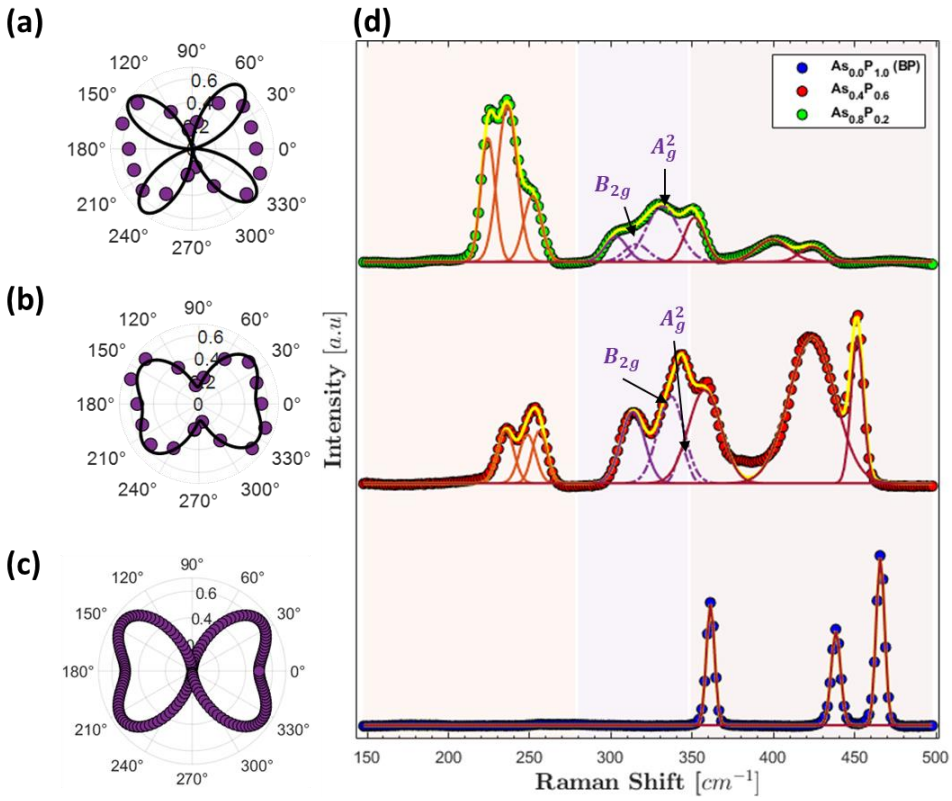

Figure 9. Comparison of the ARP Raman intensities of the in-plane As-P vibrational modes for b-$As_{0.4}P_{0.6}$ sample in the parallel configuration with the fits from the intensity function derived using Raman tensors for an orthorhombic crystal structure considering only one B_{2g} mode (a) and the superposition of two modes (b). The theoretical calculation considering the superposition of the two modes is also shown in (c). (d) the Raman shift with fine-tuned fitting parameters to include B_{2g} and A_g^2 As-P modes.

4. CONCLUSION

The polarized Raman spectroscopy is a powerful tool for determining the crystallographic orientation of materials, especially 2D materials with in-plane anisotropy. In this study, the polarization-resolved Raman spectra of b-As_xP_{1-x} flakes with varying Arsenic concentration (x =

0, 0.4, and 0.8) were studied using linearly polarized Raman scattering, especially to identify the in plane and out of plane vibrational modes of As-P. A clear polarization dependence of the Raman behavior was observed in Raman intensity of all the P-P, As-P, and As-As modes and was confirmed by the first-principles calculations. The observed angle-dependent Raman intensities could be related to the structure of the Raman tensors of each peak. In particular, the Raman intensities corresponding to the As-P vibration modes were studied in detail. The out of plane As-P mode (A_g^1) was clearly identified in the range of 303-313 cm^{-1} for the two b-As_xP_{1-x}. However, the butterfly shape observed in the polar plot around 350 cm^{-1} was interpreted as the combination of the two in-plane vibrations along the armchair and the zigzag directions. This work allows unambiguous assignment of the A_g^1, B_{2g} and A_g^2 modes of the As-P vibrational modes and the importance of the consideration of the superposition of the in-plane B_{2g} and A_g^2 modes. Such study can be utilized to further characterize the anisotropic structural properties and analyze the local distribution of As and P atoms in b-As_xP_{1-x} alloys which will play key roles in electronic and optical properties. More importantly, this formalism can be further extended to other two-dimensional alloyed structures.

SUPPORTING INFORMATION

(a) Calculated normalized intensity of ARP Raman spectra of BP modes; (b) Optical Images of b-AsxP1-x flakes used in this study; (c) Raman active modes of two b-As_xP_{1-x} alloys: b-$As_{0.375}$ $P_{0.625}$ and b-$As_{0.75}$ $P_{0.25}$; (d) Calculated Raman shifts of b-As_xP_{1-x} alloys ; (e) Calculated parameters for angle dependence Raman intensity analysis; (f) Values of fitted parameters in

angle dependence Raman intensity for BP, and its alloys used in this study; (g) Comparison of density functional theory (DFT) results ~~along~~ with experimental results.

ACKNOWLEDGMENTS

This work was supported by the U.S. Department of Energy, Office of Science, Basic Energy Sciences, under Award # DE-SC0024131.

AUTHOR INFORMATION

Corresponding Authors

***** Ming Yu (ming.yu.1@louisville.edu)

***** Jacek B. Jasinski (jacek.jasinski@louisville.edu)

REFREENCE

1. Castellanos-Gomez, A., et al., *Isolation and characterization of few-layer black phosphorus.* 2D Materials, 2014. **1**(2): p. 025001.
2. Xia, F., H. Wang, and Y. Jia, *Rediscovering black phosphorus as an anisotropic layered material for optoelectronics and electronics.* Nature communications, 2014. **5**(1): p. 4458.
3. Akhtar, M., et al., *Recent advances in synthesis, properties, and applications of phosphorene.* npj 2D Materials and Applications, 2017. **1**(1): p. 5.
4. Tran, V., et al., *Layer-controlled band gap and anisotropic excitons in few-layer black phosphorus.* Physical Review B, 2014. **89**(23): p. 235319.
5. Akahama, Y., S. Endo, and S.-i. Narita, *Electrical properties of black phosphorus single crystals.* Journal of the Physical Society of Japan, 1983. **52**(6): p. 2148-2155.
6. Qiao, J., et al., *High-mobility transport anisotropy and linear dichroism in few-layer black phosphorus.* Nature communications, 2014. **5**(1): p. 4475.
7. Wang, X. and S. Lan, *Optical properties of black phosphorus.* Advances in Optics and photonics, 2016. **8**(4): p. 618-655.
8. Jeon, S.G., et al., *Thickness-dependent and anisotropic thermal conductivity of black phosphorus nanosheets.* Nanoscale, 2018. **10**(13): p. 5985-5989.
9. Yao, J. and G. Yang, *2D layered material alloys: Synthesis and application in electronic and optoelectronic devices.* Advanced Science, 2022. **9**(1): p. 2103036.
10. Singh, A.K., et al., *Review of strategies toward the development of alloy two-dimensional (2D) transition metal dichalcogenides.* Iscience, 2021. **24**(12).
11. Han, R., et al., *Properties and photodetector applications of two-dimensional black arsenic phosphorus and black phosphorus.* Science China Information Sciences, 2021. **64**: p. 1-14.
12. Karki, B., et al., *Structural and thermoelectric properties of black arsenic–phosphorus.* ACS Applied Energy Materials, 2020. **3**(9): p. 8543-8551.
13. Liu, B., et al., *Black arsenic–phosphorus: layered anisotropic infrared semiconductors with highly tunable compositions and properties.* Advanced Materials, 2015. **27**(30): p. 4423-4429.
14. Shojaei, F. and H.S. Kang, *Electronic structure and carrier mobility of two-dimensional α arsenic phosphide.* The Journal of Physical Chemistry C, 2015. **119**(34): p. 20210-20216.
15. Luxa, J., et al., *Black phosphorus–arsenic alloys for lithium ion batteries.* FlatChem, 2020. **19**: p. 100143.
16. Abu, U.O., et al., *Degradation Studies of Air-Exposed Black Phosphorous and Black Arsenic Phosphorous.* ChemEngineering, 2023. **7**(2): p. 18.
17. Cong, X., et al., *Application of Raman spectroscopy to probe fundamental properties of two-dimensional materials.* npj 2D Materials and Applications, 2020. **4**(1): p. 13.
18. Wu, J.-B., et al., *Resonant Raman spectroscopy of twisted multilayer graphene.* Nature Communications, 2014. **5**(1): p. 5309.
19. Li, X.-L., et al., *Layer-Number Dependent Optical Properties of 2D Materials and Their Application for Thickness Determination.* Advanced Functional Materials, 2017. **27**(19): p. 1604468.
20. Zhao, W., et al., *Charge transfer and optical phonon mixing in few-layer graphene chemically doped with sulfuric acid.* Physical Review B, 2010. **82**(24): p. 245423.
21. Dai, Z., L. Liu, and Z. Zhang, *Strain Engineering of 2D Materials: Issues and Opportunities at the Interface.* Advanced Materials, 2019. **31**(45): p. 1805417.

22. Jin, M., et al., *Raman tensor of WSe2 via angle-resolved polarized Raman spectroscopy.* The Journal of Physical Chemistry C, 2019. **123**(48): p. 29337-29342.
23. Liu, Y., et al., *Angle-resolved polarized Raman spectra of the basal and edge plane of MoS 2.* Optics Express, 2021. **29**(21): p. 32818-32825.
24. Pimenta, M.A., et al., *Polarized Raman spectroscopy in low-symmetry 2D materials: angle-resolved experiments and complex number tensor elements.* Physical Chemistry Chemical Physics, 2021. **23**(48): p. 27103-27123.
25. Kim, J., et al., *Anomalous polarization dependence of Raman scattering and crystallographic orientation of black phosphorus.* Nanoscale, 2015. **7**(44): p. 18708-18715.
26. Zhu, Y., et al., *Raman tensor of layered black phosphorus.* PhotoniX, 2020. **1**(1): p. 17.
27. Lin, M.-L., et al., *Understanding angle-resolved polarized Raman scattering from black phosphorus at normal and oblique laser incidences.* Science Bulletin, 2020. **65**(22): p. 1894-1900.
28. Pradhan, N.R., et al., *Raman and electrical transport properties of few-layered arsenic-doped black phosphorus.* Nanoscale, 2019. **11**(39): p. 18449-18463.
29. Chen, Y., et al., *Black arsenic: a layered semiconductor with extreme in-plane anisotropy.* Advanced materials, 2018. **30**(30): p. 1800754.
30. Vithanage, D., et al., *Electrochemical Li intercalation in b-AsyP1− y alloys: In-situ Raman spectroscopy study.* Journal of Alloys and Compounds, 2023. **968**: p. 171849.
31. Liu, X.-L., et al., *Different angle-resolved polarization configurations of Raman spectroscopy: A case on the basal and edge plane of two-dimensional materials.* Chinese Physics B, 2017. **26**(6): p. 067802.
32. Wu, J., et al., *Identifying the Crystalline Orientation of Black Phosphorus Using Angle-Resolved Polarized Raman Spectroscopy.* Angewandte Chemie International Edition, 2015. **54**(8): p. 2366-2369.
33. Kresse, G. and J. Furthmüller, *Efficient iterative schemes for ab initio total-energy calculations using a plane-wave basis set.* Physical review B, 1996. **54**(16): p. 11169.
34. Blöchl, P.E., *Projector augmented-wave method.* Physical review B, 1994. **50**(24): p. 17953.
35. Perdew, J.P., K. Burke, and M. Ernzerhof, *Generalized gradient approximation made simple.* Physical review letters, 1996. **77**(18): p. 3865.
36. Perdew, J.P., et al., *Atoms, molecules, solids, and surfaces: Applications of the generalized gradient approximation for exchange and correlation.* Physical review B, 1992. **46**(11): p. 6671.
37. Gonze, X., *First-principles responses of solids to atomic displacements and homogeneous electric fields: Implementation of a conjugate-gradient algorithm.* Physical Review B, 1997. **55**(16): p. 10337.
38. Monkhorst, H.J. and J.D. Pack, *Special points for Brillouin-zone integrations.* Physical review B, 1976. **13**(12): p. 5188.
39. Grimme, S., *Semiempirical GGA-type density functional constructed with a long-range dispersion correction.* Journal of computational chemistry, 2006. **27**(15): p. 1787-1799.
40. Porezag, D. and M.R. Pederson, *Infrared intensities and Raman-scattering activities within density-functional theory.* Physical Review B, 1996. **54**(11): p. 7830.
41. Stauffer, A.F.a.S., *vasp_raman.py*. 2013.
42. Zhu, Z., J. Guan, and D. Tománek, *Structural Transition in Layered As1–x P x Compounds: A Computational Study.* Nano letters, 2015. **15**(9): p. 6042-6046.
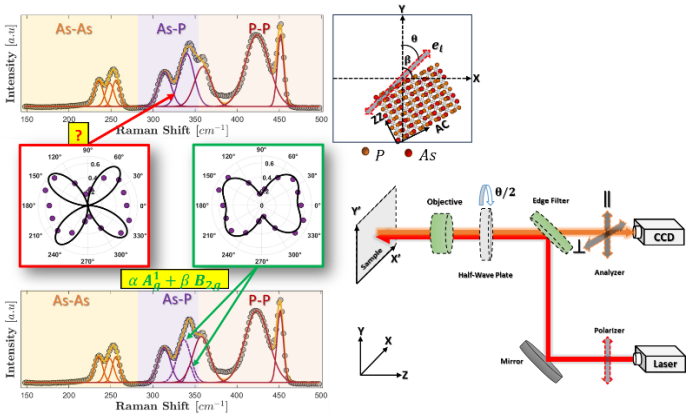
Graphical Abstract